ACS NANO

www.acsnano.org

ARTICLE

Atomically Thin Bilayer Janus Membranes for Cryo-electron Microscopy

Liming Zheng, Nan Liu, Ying Liu, Ning Li, Jincan Zhang, Chongzhen Wang, Wenqing Zhu, Yanan Chen, Dongchen Ying, Jie Xu, Zi Yang, Xiaoyin Gao, Jilin Tang, Xiaoge Wang, Zibin Liang, Ruqiang Zou, Yuzhang Li, Peng Gao, Xiaoding Wei,* Hong-Wei Wang,* and Hailin Peng*

Cite This: *ACS Nano* 2021, 15, 16562−16571

Read Online

ACCESS | Metrics & More | Article Recommendations | Supporting Information

ABSTRACT: **Cryo-electron microscopy (cryo-EM) has emerged as a vital tool to reveal the native structure of beam-sensitive biomolecules and materials. Yet high-resolution cryo-EM analysis is still limited by the poorly controlled specimen preparation and urgently demands a robust supporting film material to prepare desirable samples. Here, we developed a bilayer Janus graphene membrane with the top-layer graphene being functionalized to interact with target molecules on the surface, while the bottom layer being kept intact to reinforce its mechanical steadiness. The ultraclean and atomically thin bilayer Janus membrane prepared by our protocol on one hand generates almost no extra noise and on the other hand reduces the specimen motion during cryo-EM imaging, thus allowing the atomic-resolution characterization of surface functional groups. Using such Janus membranes in cryo-EM specimen preparation, we were able to directly image the lithium dendrite and reconstruct macromolecules at near-atomic resolution. Our results demonstrate the bilayer Janus design as a promising supporting material for high-resolution cryo-EM and EM imaging.**

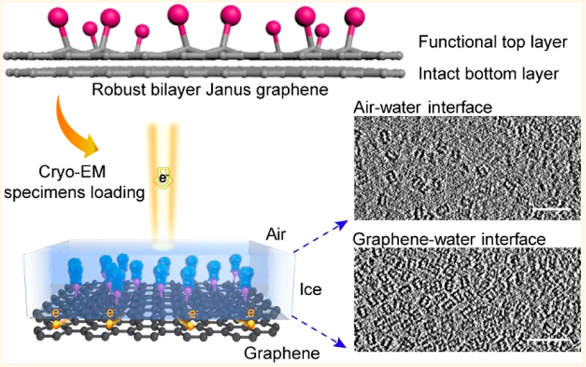

KEYWORDS: *bilayer graphene, Janus, mechanical robust, cryo-EM, near-atomic resolution*

Technological breakthroughs in cryo-electron microscopy (cryo-EM) have made it a powerful tool to determine the close-to-native structures of beam-sensitive materials, including biological macromolecules,[1−4] lithium battery materials,[5−7] metal−organic frameworks (MOFs),[8] and organic−inorganic halide perovskites.[9] Compared with the rapid technique developments in data collection and processing, cryo-EM specimen preparation remains largely unchanged and is still a trial-and-error process, which has become a primary barrier to high-resolution cryo-EM analysis.[10,11]

To facilitate rapid and reliable specimen preparation for high-quality EM imaging, graphene, as a promising support material, has recently drawn wide attention.[11−23] As an atomically thin support film, graphene can minimize the background noise and avoid adsorption of target molecules at the air−water interface.[12−16] The interaction of protein particles with the air−water interface often leads to sample denaturation or preferential orientation. One of the desirable approaches to promote cryo-EM specimen quality is to anchor the samples on the affinity-modified graphene surfaces.[10,15,20] However, several long-standing issues still limit the wide application of graphene films in high-resolution cryo-EM: (1) The cryo-EM community conventionally uses plasma treatment or chemical modification to generate hydrophilic affinity graphene monolayer. These treatments on a graphene basal plane, unfortunately, will damage the sp^2 carbon network of the graphene lattice, thus severely degrading mechanical and electrical robustness of the supporting film during further specimen preparation and data collection.[24,25] (2) Although the growth of high-quality large-area graphene film by chemical vapor deposition (CVD) has been reported,[26] the accessibility of a robust graphene source is still a practical barrier in the EM community. (3) Contaminations introduced during graphene synthesis, the commonly used polymer-mediated graphene transfer, or graphene modification may result in non-negligible background noise and make graphene functionalization less controllable.[13,20,27] (4) The surface chemistry of affinity

Received: July 22, 2021
Accepted: September 23, 2021
Published: September 27, 2021

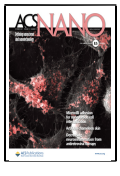

https://doi.org/10.1021/acsnano.1c06233
ACS Nano 2021, 15, 16562−16571

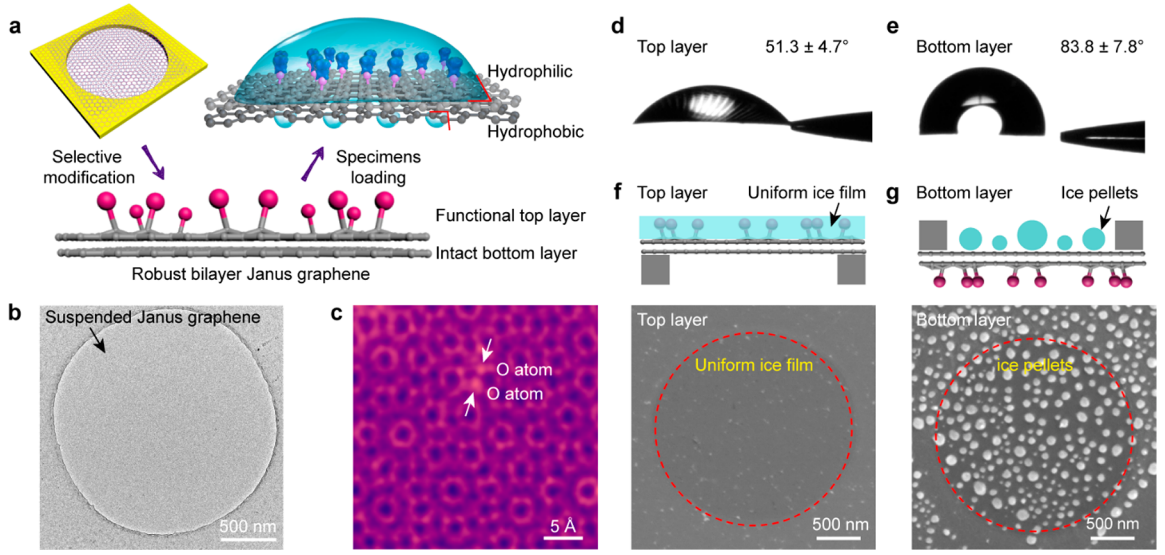

Figure 1. Ultraclean bilayer Janus graphene membranes with asymmetric wettability. (a) Schematic illustration of bilayer Janus graphene membranes. The top layer is functionalized to improve the wettability of graphene and anchor the particles, while the bottom layer is intact to maintain the excellent mechanical and electrical properties of graphene. (b) Representative TEM micrograph of suspended bilayer Janus graphene, showing the ultraclean graphene surface. (c) Atomic-resolution STEM image of bilayer Janus graphene with oxygen-pair configuration. (d, e) Typical optical images revealing the hydrophilic top layer of Janus graphene grid with a water contact angle of ~51.3° (d) and hydrophobic bottom layer with a water contact angle of ~83.8° (e). (f) Schematic (top row) and a typical cryo-SEM image (bottom row) showing a uniform ice film on the top layer of bilayer Janus graphene. (g) Schematic (top row) and a typical cryo-SEM image (bottom row) showing the heterogeneous ice pellets on the bottom layer of bilayer Janus graphene.

graphene and the chemical functional groups in functionalized graphene lattice are still poorly characterized at the atomic scale.[10,28] Therefore, the development of background-free membranes with precisely functionalized surface and robust support base will be critical for more general application in cryo-EM.

Here we present an atomically thin bilayer Janus graphene support for atomic-resolution cryo-EM. In this bilayer Janus structure, the top layer is tailored with functional groups, which are used to render hydrophilic graphene and attract the target molecules. In contrast, the bottom layer of graphene remains intact so that the mechanical and electrical robustness of graphene is largely maintained. The bilayer Janus graphene exhibits an ultraclean surface, enabling the direct characterization of surface functional groups and a Li dendrite sample at the atomic scale. We show that such a Janus graphene design facilitates the reduction of beam-induced specimen motion during cryo-EM imaging and allows the single-particle reconstruction of bacterial 50S ribosome at 2.7 Å resolution.

RESULTS AND DISCUSSION

Ultraclean Bilayer Janus Graphene with Asymmetric Wettability. Compared with monolayer graphene, bilayer and multilayer graphenes offer an additional degree of freedom in layer number, allowing the precise chemical modification layer by layer. Besides, the bilayer graphene produces a very low background in atomic-resolution EM where individual atoms can be recognized at high contrast (Supporting Information Figure S1). These properties make the bilayer graphene a promising candidate for specimen support in EM. To render the bilayer graphene with desired hydrophilicity and functionality, we selectively modify the topmost layer with oxygen-containing groups, forming a bilayer Janus structure with an intact bottom layer (Figure 1a). The bilayer Janus graphene not only enables efficient specimen loading but also maintains its superior mechanical strength and conductivity, despite the lattice of top-layer graphene being partially disordered by the functional groups (Figure 1a).

To fabricate the ultraclean bilayer Janus graphene grids, we adopted a polymer-free transfer strategy. First, we used the high H_2/CH_4 ratio (1000:1) and high pressure (2000 Pa) to grow bilayer graphene on the copper foil by CVD. The high H_2/CH_4 ratio enabled the growth of a second graphene layer underneath the existing monolayer graphene, yet the growth rate of the bilayer graphene was slow.[29] Thus, we increased the high pressure in the CVD system to enhance the growth rate and coverage of bilayer graphene. To avoid the polymer contaminations during the bilayer graphene transfer, we directly attached the TEM grid (Quantifoil, Au-300 mesh-R1.2/1.3) onto the graphene/copper surface assisted with isopropanol (IPA).[30] Then the copper was etched off from grid/graphene/copper composite by $(NH_4)_2S_2O_8$ solution. After being rinsed and dried, the graphene grid with a clean surface was obtained. The individual carbon atoms and Moiré pattern were distinctly resolved at an atomic resolution of sub-Å by scanning transmission electron microscopy (STEM), revealing the ultraclean surface of bilayer graphene (Figure S2). To prepare the bilayer Janus graphene, we used a low-energy oxygen plasma (power, 80 W; time, 18 s) to modify the bilayer graphene surface. The suspended bilayer Janus graphene exhibited a uniform surface with almost no polymer residues (Figure 1b). O atom in the graphene lattice can be clearly identified due to its heavier mass compared to C in the high-angle annular dark field (HAADF) STEM imaging mode (Figure 1c and Figure S3).

The bilayer Janus membrane exhibits bifacial anisotropic wettability due to the asymmetric modification of bilayer graphene. Owing to the introduction of polar oxygen-containing groups, the top surface of bilayer Janus graphene grid was more hydrophilic with a water contact angle (WCA)

https://doi.org/10.1021/acsnano.1c06233
ACS Nano 2021, 15, 16562−16571

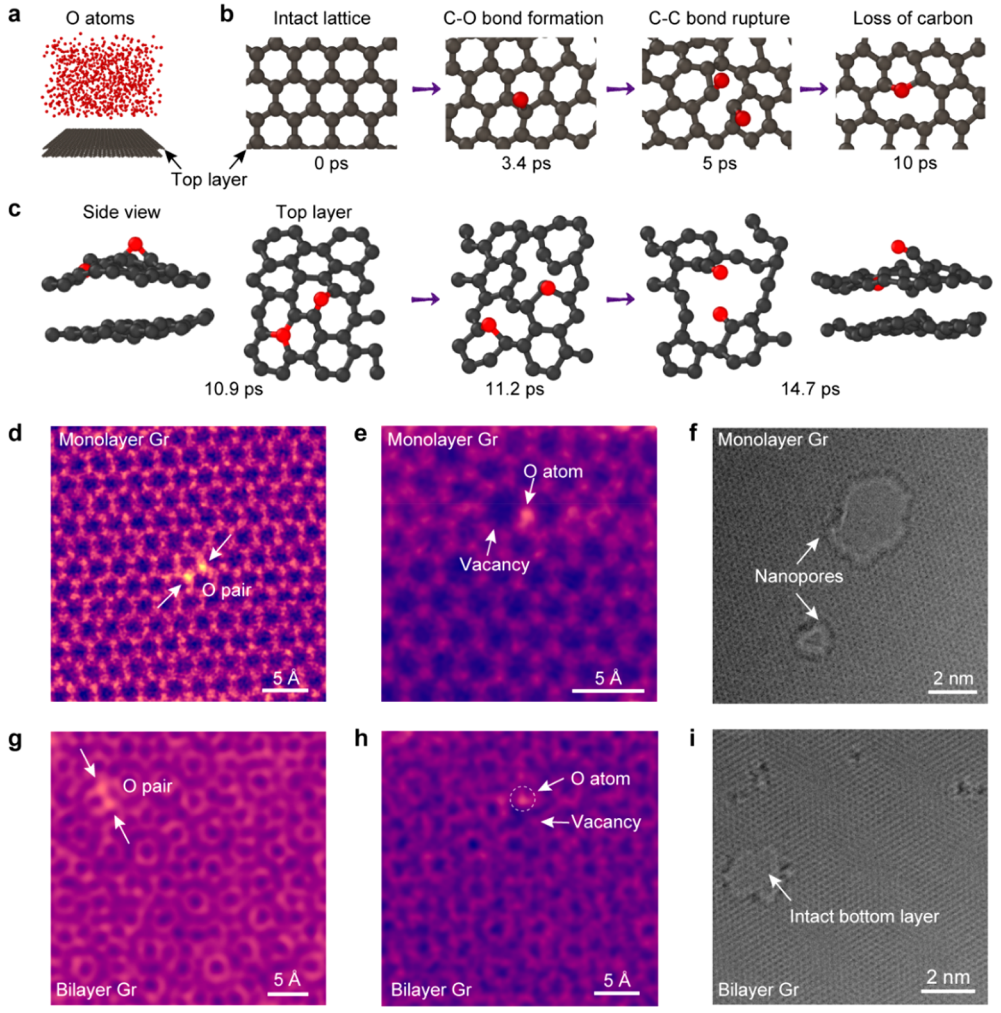

Figure 2. Surface structure manipulation of bilayer Janus membranes. (a) Initial configuration of the molecular dynamics model consisting of bilayer graphene sheet (black color) and oxygen atoms (red color). (b) Snapshots of simulated dynamic process showing the C−O bond formation, C−C bond rupture, and loss of carbon in the top layer of bilayer graphene. (c) Defect coalescence and nanopore formation in the top-layer lattice with a maintained intact bottom layer. (d−f) High-resolution STEM and TEM images showing the oxygen pair (d), oxygen-containing vacancy (e), and nanopore (f) in monolayer graphene lattice. (g−i) High-resolution STEM and TEM images showing the oxygen pair (g), oxygen-containing vacancy (h), and nanopore (i) on the top layer of bilayer Janus graphene.

of ∼51.3° (Figure 1d and Figure S4), whereas the opposite side of the grid with intact bottom layer of graphene showed a hydrophobic surface with a WCA of ∼83.8° (Figure 1e and Figure S4). In consideration of the wetting transparency of graphene,[31−33] we further investigated the intrinsic wettability of suspended graphene membrane to exclude the influence of the supporting substrate. We sprayed water vapor onto the Janus graphene membrane using a humidifier, and then the graphene was immediately cooled to liquid-nitrogen temperature and subsequently examined under cryo-scanning electron microscopy (cryo-SEM). We observed ice films spreading uniformly on the top-layer graphene membrane (Figure 1f and Figure S5) but an uneven distribution of ice pellets on the bottom layer with variable dimensions (Figure 1g and Figure S6). These observations indicated a distinct bifacial anisotropic wettability of bilayer Janus graphene.

Furthermore, the distribution of soluble protein macromolecules can be used as a wettability indicator since soluble proteins tend to stay on a hydrophilic surface.[17] We found that, on the top layer of Janus graphene, 20S proteasomes were distributed as monodispersed particles at a high concentration (Figure S7a). In contrast, few 20S proteasomes were observed on the bottom layer (Figure S7b). Therefore, the functional top layer of suspended Janus graphene is efficiently hydrophilic to load biological macromolecules. In contrast, the bottom-layer graphene remains hydrophobic and impervious to the covalent modification of the top layer.

Structural Engineering of Bilayer Janus Membranes. Bilayer Janus membranes were created through asymmetric modification of bilayer graphene films with oxygen plasma. To investigate the reaction dynamics between oxygen plasma and bilayer graphene, we carried out molecular dynamics (MD) simulation to reveal the bonding interaction in the oxygen-plasma treatment. In the initial stage of MD simulation, oxygen atoms were placed above the bilayer graphene sheets (Figure 2a). Subsequently, the oxygen atoms were chemisorbed on the top-layer graphene and C−O bonds were first formed (Figure 2b). As the number of chemisorbed oxygen atoms increased, the rupture of C−C bonds and loss of carbon occurred, leading to the formation of carbonyl, ether groups, and vacancies in graphene lattice (Figure 2b). With the increased defect density, the adjacent vacancies would coalesce and lead to an extended

https://doi.org/10.1021/acsnano.1c06233
ACS Nano 2021, 15, 16562−16571

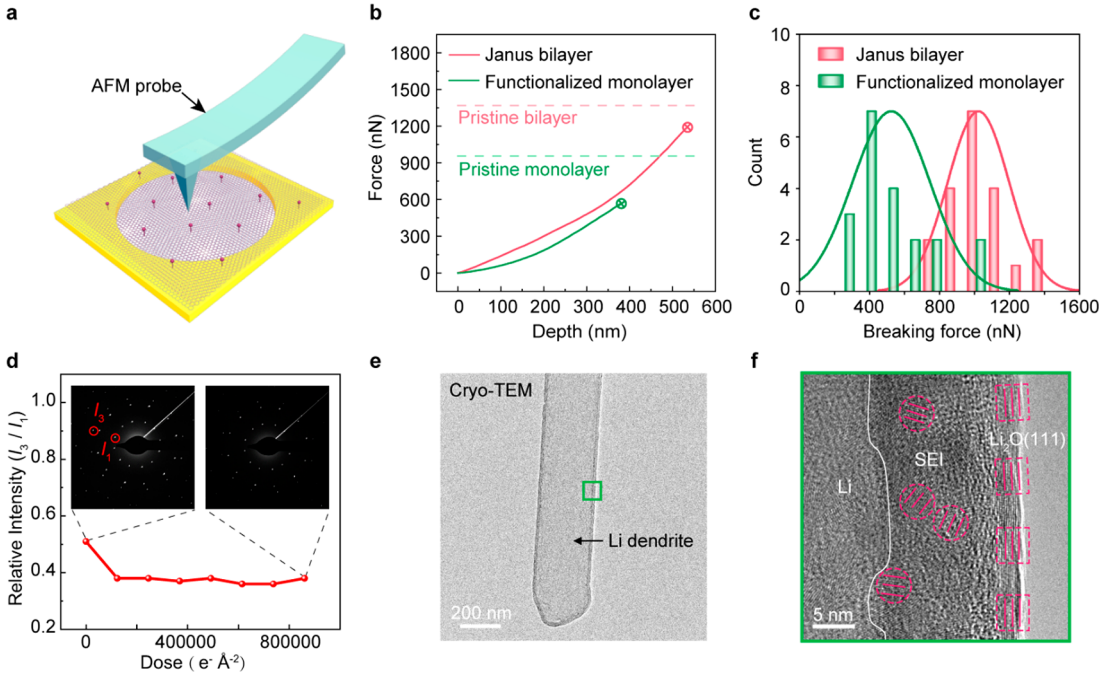

Figure 3. Mechanical robustness and electron-beam resistance of bilayer Janus membranes. (a) Schematic illustration of AFM indentation experiment. (b) Typical loading curves for bilayer Janus and functional monolayer graphene. The dotted lines represent the average breaking force of pristine bilayer (red) and pristine monolayer graphene (green) for comparison. (c) Histograms of breaking forces for bilayer Janus and functional monolayer graphene. (d) Robustness of bilayer Janus graphene under the electron irradiation, characterized by the intensity ratio of the third-order Bragg reflection (I_3) to the first-order (I_1) from SAED patterns of graphene as a function of electron dose. Insets: SAED patterns from the same position of bilayer Janus graphene at indicated dose points. (e) Cryo-TEM image of Li dendrite on the bilayer Janus graphene. (f) High-resolution image of the green region marked in panel e showing the interface between SEI and Li metal. The crystalline grains dispersed in the amorphous matrix are identified to be Li_2O by matching the lattice spacings.

nanopore in the top layer, while the bottom layer remained intact, as shown in the side view of bilayer Janus graphene (Figure 2c).

Our experimental results were in good agreement with the theoretical simulation. Raman spectroscopy was often used to investigate the structure disorder in the sp^2 network of Janus graphene.[34] As the plasma-treatment time was prolonged, the intensity of the D band (~1350 cm^{-1}) increased, indicating an accumulation of functional groups in the graphene lattice (Figure S8). By controlling the plasma-treatment time, we can manipulate the surface structure of bilayer Janus graphene. With a plasma treatment of ~18 s, the oxygen-atom point defects including oxygen pair and oxygen-containing vacancy were observed in the top layer of bilayer graphene using atomic-resolution STEM images (Figures 1c and 2g,h). Interestingly, similar configurations were also often found in plasma-treated monolayer graphene (Figure 2d,e) and graphene oxide,[35] where two oxygen atoms substituted neighboring carbon atoms for oxygen-pair configuration and oxygen atoms were coordinated at the edge of a vacancy. With the longer treatment time of ~30 s, nanopores appeared in the monolayer graphene lattice (Figure 2f) and the top layer of bilayer graphene (Figure 2i), while the bottom layer remained intact (Figure 2i), consistent with the MD simulations.

Robust Bilayer Janus Membranes. To evaluate the mechanical strength of suspended bilayer Janus graphene, we performed atomic force microscope (AFM) nanoindentation using a single-crystal diamond probe to indent the center of the suspended graphene membranes on the grid (Figure 3a). The force *vs* indentation depth curves were obtained until the graphene ruptured (Figure 3b). Thanks to the intact bottom layer, the bilayer Janus graphene maintained its integrity and its strength is only slightly lower than that of pristine bilayer graphene (Figure 3b and Figure S9). In contrast, the breaking force of monolayer graphene decreased significantly after treatment with the same plasma treatment (Figure 3b and Figure S10). It is worth noting that the average breaking force of bilayer Janus graphene is almost twice as large as that of the treated monolayer graphene (Figure 3c). The mechanical robustness of bilayer Janus graphene guaranteed a record high coverage ratio (~99.8%) for the grid (Figure S11), which would facilitate high-efficiency specimen preparation and EM data collection.

Meanwhile, the bilayer Janus graphene exhibited excellent stability under electron-beam irradiation, as revealed by the electron-dose resistance characterization. The graphene membrane was continuously radiated at the same position under the electron beam with a dose rate of ~204.76 ($e^-/Å^2$)/s in a Tecnai F20 microscopy (200 kV), and we collected its selected area electron diffraction patterns on a CCD camera from 0 to 70 min. As shown in Figure 3d, although bilayer Janus graphene was continuously irradiated with a high electron dose of ~800,000 $e^-Å^{-2}$ at the same position, the diffraction spots of the selected area electron diffraction (SAED) of the graphene lattice remained sharp. The intensity ratio of the third-order Bragg reflections (I_3) to the first-order ones (I_1) of SAED patterns only showed a minor decay with the electron-dose accumulation, indicating good preservation of the high-quality graphene lattice during the electron irradiation (Figure 3d and Figure S12).

Due to the excellent mechanical robustness and stability, the Janus graphene contributed to the high-resolution imaging of

https://doi.org/10.1021/acsnano.1c06233
ACS Nano 2021, 15, 16562−16571

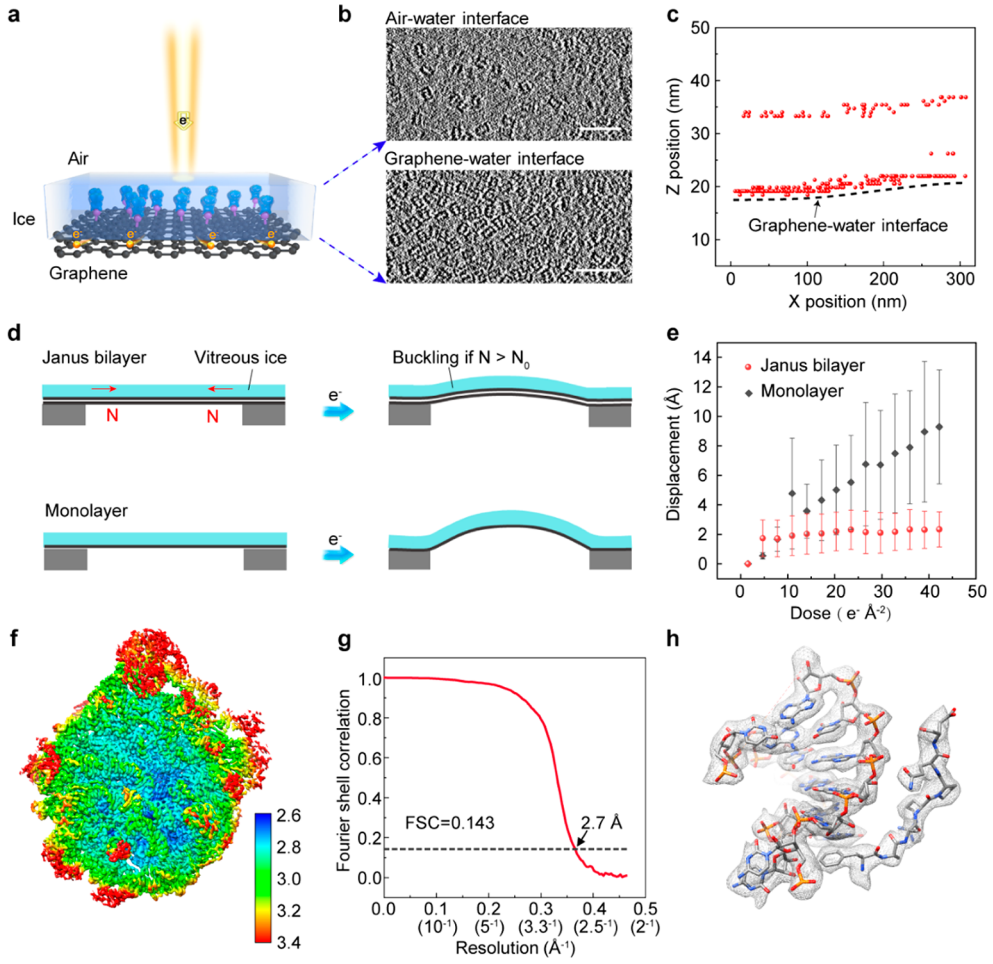

Figure 4. Bilayer Janus membranes for high-resolution cryo-EM structure determination. (a) Schematic representation of biological macromolecules (in blue color) adsorbed at the graphene−water interface. (b) Representative cryo-ET sections showing the distribution of 20S proteasome particles at the air−water interface (top row) and graphene−water interface (bottom row), respectively. (c) Spatial distribution of 20S proteasome particles embedded in vitrified ice indicated by cryo-ET. Each red spot represents one 20S particle. (d) Schematics showing the buckling of the ice film on the bilayer Janus and monolayer graphene, respectively. The buckling occurs if the compressive stress (N) in ice exceeds a critical compression (N_0). (e) Particle motion on the bilayer Janus and monolayer graphene under electron-beam radiation. Each point represents the average displacement of thousands of 20S proteasome particles, and the error bars result from the observed values of 3 different times. (f) Overall density of the reconstructed 50S ribosome, colored by local resolution distribution. The color bar is shown (unit, Å). (g) Fourier shell correlation (FSC) plot of the 50S ribosome reconstruction. The resolution of 2.7 Å was estimated according to the criterion of FSC = 0.143. (h) Selected density regions with the corresponding atomic models docked. The bases and phosphodiester bonds of RNA and side chains of amino acids can be clearly recognized.

beam-sensitive Li dendrite. Just like the protein denaturation risk at the air−water interface, Li metal would rapidly corrode after short air exposure.[36] Thus, we directly deposited Li dendrites onto the Janus graphene grid in a Li battery to preserve the native state of Li dendrite using a reported cryo-transfer method originated from structural biology.[5] As shown in Figure 3e, the Janus graphene provided a high contrast for the light Li metal. The solid electrolyte interphase (SEI) layer formed during battery cycling can be clearly identified at the periphery of Li dendrite. The SEI layer resembled a mosaic structure with Li oxide heterogeneously distributed in the organic amorphous matrix (Figure 3f and Figure S13), agreeing with previous observations[5] and demonstrating the potential of bilayer Janus graphene for more general cryo-EM applications.

Bilayer Janus Membranes for High-Resolution Cryo-EM Structural Determination. To verify if the bilayer Janus graphene membranes are suitable for high-resolution single-particle cryo-EM, we prepared cryo-EM specimens of the *Thermoplasma acidophilum* 20S proteasome and *Escherichia coli* 50S ribosome on our bilayer Janus graphene grids. As illustrated by cryo-electron tomography (cryo-ET), the 20S proteasome particles in vitrified ice tended to be mostly adsorbed to the graphene−water interface (Figure 4a,b). The particle adsorption preference for Janus graphene over the air−water interface might help to prevent the denaturation and preferential orientation problem in cryo-EM specimens.[16,37,38] Moreover, the hydrophilic bilayer Janus graphene support allowed us to achieve a thin ice layer with a thickness of ∼25 nm (Figure 4c), which is suitable to embed protein particles without introducing much extra ice noise.[28]

We also measured the beam-induced particle motion on the bilayer Janus graphene during cryo-EM imaging. The particle motion degrades image quality and results in the most information loss in cryo-EM.[39] According to the theory of ice movement,[39] the particle motion is mainly caused by the

https://doi.org/10.1021/acsnano.1c06233
ACS Nano 2021, 15, 16562−16571

buckling of the ice layer (Figure 4d). Once the compression in the ice layer exceeds a threshold value N_0, the ice layer will buckle. The lowest critical compression, N_0, is described by

$$N_0 = A\frac{Eh^3}{12a^2(1-\upsilon^2)}$$

where E is the effective Young's modulus of the graphene and ice composite, a represents the radius of the uniform homogeneous ice plate, h is the thickness of the ice, υ is the Poisson ratio, and A is a constant depending on the boundary conditions of ice plate. Moreover, on the basis of the rule of mixtures,[40] the composite Young's modulus of graphene and ice, $E_{G\text{-}Ice}$, is

$$E_{G\text{-}Ice} = E_G\frac{t_G}{t_G + t_{Ice}} + E_{Ice}\frac{t_{Ice}}{t_G + t_{Ice}}$$

Here, E_{Ice} and E_G are Young's moduli for ice (~1 GPa) and graphene (~1000 GPa), respectively. t_{Ice} and t_G are the thicknesses of ice (~25 nm) and graphene (0.34 nm for monolayer and 0.68 nm for bilayer), respectively. Thus, the effective Young's modulus of bilayer Janus graphene and ice $E_{Janus\text{-}Ice}$, is estimated to be ~27.5 GPa, while that of monolayer graphene and ice, $E_{Mono\text{-}Ice}$, is ~14.4 GPa. Therefore, we speculate that N_0 in the ice on bilayer Janus graphene is notably larger than that on monolayer graphene, which means the particle motion can be reduced by increasing the thickness of supporting film (Figure 4d). To verify this hypothesis, we recorded the motion of proteins on the bilayer Janus and monolayer graphene and found that the beam-induced motion indeed decreased with the increased layer number of graphene (Figure 4e). Similar results were observed when increasing the thickness of amorphous carbon film,[41,42] further proving that the enhanced mechanical robustness is conducive to reducing the beam-induced motion.

A cryo-specimen of the 50S ribosome on the bilayer Janus graphene membranes showed a monodispersed distribution with a high density (Figure S14). Two-dimensional class averages of these particle images displayed fine details of the 50S ribosome in different views (Figure S14). After three-dimensional (3D) classification and autorefinement, we got a 3D reconstruction of the 50S ribosome at a resolution of 2.7 Å (Figure 4f,g), which is good enough to assign the bases of RNA and side chains of amino acids in the EM map (Figure 4h). The final atomic model is in good agreement with the previously reported result.[43]

CONCLUSIONS

In conclusion, on the basis of the bilayer graphene with an additional degree of freedom, we selectively modified the topmost graphene surface as a functional layer for efficient sample adsorption. The resultant bilayer Janus graphene remained background-free for atomic-resolution imaging, allowing the precise characterization of surface atomic structures. The oxygen-pair configuration and oxygen-containing vacancy are frequently observed on the top layer of Janus graphene, which may help get insight into the interactions between particles and graphene supports. Meanwhile, the bilayer Janus graphene maintained the mechanical robustness of graphene, which is beneficial to the reduction of beam-induced motion based on the theory of ice movement. Using such bilayer Janus graphene as supporting film for structure determination by single-particle cryo-EM, a near-atomic-resolution reconstruction of 50S ribosome can be achieved.

Considering that the plasma-treated carbon films have been used for a long time in the EM community, a similar plasma treatment on the robust bilayer graphene will be widely practical to prepare hydrophilic graphene support. The densities of active sites are controllable by changing the treatment time according to our MD simulations and Raman spectroscopy. Moreover, the bilayer Janus graphene can provide a versatile platform for further modification with multiple chemical ligands. Besides being a specimen support for high-resolution EM, the Janus graphene membranes also hold promise in proton separations, biosensing, and electronic devices.

EXPERIMENTAL SECTION

Growth of Bilayer Graphene Films. The bilayer graphene film was grown on commercial copper foil (Alfa-Aesar No. 46365) by low-pressure chemical vapor deposition (LPCVD, Figure S16). The copper foil was first polished in electrolyte solution composed of phosphoric acid and ethylene glycol (v/v = 3:1) for 30 min to clean the copper foil. Then the copper foil was placed on a quartz substrate in LPCVD system and annealed at 1030 °C for 30 min in 100 sccm H_2. To grow bilayer graphene film, a flow of 1000 sccm H_2 and 1 sccm CH_4 was subsequently pumped into the LPCVD system with a pressure of ~2000 Pa and maintained for 0.5−1 h. After growth, the graphene film on the copper foil was rapidly cooled to ~500 °C. Then the supply of H_2 and CH_4 were stopped, and 500 sccm CO_2 was introduced into the LPCVD system to clean the bilayer graphene surface at ~500 °C for 3 h.[27]

To increase the growth rate and coverage of bilayer graphene, we used the H_2/CH_4 ratio of 1000:1 and pressure of 2000 Pa in the CVD system, and the coverage of bilayer graphene was more than 80% (Figure S15). In contrast, the H_2/CH_4 ratio and pressure for monolayer graphene growth were 100:1 and 100 Pa, respectively.

Preparation of Janus Bilayer Graphene Membranes. To avoid polymer contamination induced in the preparation process, the clean bilayer graphene grids were fabricated according to the polymer-free clean transfer method of monolayer graphene single-crystal films, as we previously reported.[30] Briefly, we placed a TEM grid (Quantifoil, Au-300 mesh-R1.2/1.3 or R2/1; UltraAuFoil, 300 mesh-R1.2/1.3) on the graphene/copper sample. Then ~10 μL of isopropanol (IPA) was dropped onto the sample. After the evaporation of IPA, the TEM grid was tightly attached to the graphene/copper. Subsequently, the grid/graphene/copper composite was gently placed on the surface of 1 mol/L $(NH_4)_2S_2O_8$ solution to etch the copper substrate. One hour later, the copper foil was completely etched off and the graphene was attached onto the surface of the grid. Then the grid was rinsed in the deionized water for three times to eliminate the inorganic salts on the graphene surface. After being dried in the air, the graphene grid was obtained.

To prepare bilayer Janus graphene membranes, the graphene grids were placed in a chamber of reactive ion etcher (Pico SLS, Diener), where the gas species, gas flow rate, treatment time, and power can be adjusted. Then a flow of 1 sccm oxygen was pumped into the chamber, and the oxygen plasma was generated with a low-energy power of 80 W. By controlling the plasma-treatment time, the bilayer Janus graphene with a desirable density of active sites can be achieved. Note that the plasma cleaner (such as PDC-32G, HARRICK PLASMA) can also be adopted as the alternative reactive ion etcher instrument, and we normally treated the graphene grids for 10−15s at the low-power mode.

Storage of Graphene Grids. To avoid the hydrocarbon or other contaminations in the air, the graphene grids were sealed in a vacuum bag with commercial plastic-envelop machine (MS175, Magic Seal), and stored in a dry vacuum reservoir.

MD Simulation. Molecular dynamics (MD) simulation in this study was carried out using the LAMMPS (large-scale atomic/

https://doi.org/10.1021/acsnano.1c06233
ACS Nano 2021, 15, 16562−16571

molecular massively parallel simulator) software package[44] to simulate the etching process of bilayer graphene. The MD results were visualized using OVITO software.[45] In the simulation, 1000 oxygen atoms were randomly dispersed within a domain of 54 Å × 63 Å × 40 Å in the middle of the whole simulation box. Then, two AB-stacked bilayer graphene sheets (with in-plane dimensions of 54 Å × 63 Å) were positioned above and below the oxygen domain, respectively (see Figure 2a. Only the bottom bilayer graphene sheet was depicted, for brevity.). The distances between oxygen and carbon atoms were managed to be at least 1 nm to avoid unrealistic carbon−oxygen bonds at the beginning. The dimensions of the simulation box were 54 Å × 63 Å × 72 Å, and periodic boundary conditions were employed. Since the model was constructed symmetrically along the oxygen-domain thickness direction, we mainly inspect and visualize the reactions between oxygen atoms and the bottom bilayer graphene sheet.

The reactive force field (ReaxFF) implemented in the LAMMPS package was employed to describe the interactions between carbon and oxygen atoms.[46] The Nosé−Hoover thermostat and barostat were used to control the temperature and pressure, and a time step of 0.2 fs was used. At first, two bilayer graphene sheets were equilibrated at 300 K for 2 ps in the isothermal−isobaric (*NPT*) ensemble to release the initial stress while all oxygen atoms were fixed. After that, random velocities were assigned to oxygen atoms corresponding to a temperature of 300 K. Then, the system ran for 30 ps in the microcanonical (*NVE*) ensemble to simulate the etching process.

Cryo-EM Specimen Preparation. For cryo-EM specimen preparation, ∼4 μL of 20S proteasome (0.3 μM) or 50S ribosome solution (0.5 μM) was pippeted onto freshly glow-discharged Jannus graphene grids and blotted by filter papers for 3−4 s in a Vitrobot (Thermo Fisher Scientific), with the temperature at 8 °C and humidity at 100%. Afterward, the grids were immediately plunge-frozen into liquid ethane at liquid-nitrogen temperature and kept in liquid nitrogen for further cryo-EM analysis.

Single-Particle Cryo-EM Data Collection and Analysis. Cryo-EM data sets were collected on an FEI Titan Krios (300 kV) TEM (Thermo Fisher Scientific) equipped with a Gatan K3 Summit direct electron detector camera. For single-particle cryo-EM reconstruction of the 50S ribosome, we acquired 3424 micrographs using AutoEMation2 software,[47] with the defocus range from −0.9 to −2 μm and pixel size of 1.08 Å. All of the micrographs were dose-dependently fractionated into 32 frames with the total dose of 50 e^- $Å^{-2}$ and motion-corrected by MotionCor2 package.[48] We next used CTFFIND4[49] to estimate the CTF parameters of every micrograph and autopicked protein particles in Relion3.1.[50] After 2D and 3D classification, particles grouped in bad classes were discarded, and 432,670 particles were left for further 3D refinement. The final reconstruction resolution was reported as 2.7 Å according to the FSC = 0.143 criterion after postprocessing in Relion3.1. 50S ribosome atomic model (PDB: 6PC6) was fit into the map in UCSF Chimera[43] using its "fit in map" function, and all of the structural figures were made by UCSF Chimera. For measuring particle displacements on the graphene membrane, the motion-corrected movies and iteratively refined particles were applied for Bayesian polishing in Relion3.0[50] to determine the particle coordinates in individual frames, which were used to calculate the root-mean-squared displacements and plotted *vs* dose. To make the conclusion statistical, we performed three measurements, every one of which was based on 2000 particles from 8 to 10 micrographs.

Cryo-electron Tomography. Cryo-ET micrograph tilt series was acquired on a Titan Krios (300 kV) TEM (Thermo Fisher Scientific) equipped with a Gatan K3 Summit direct electron detector camera and obtained from +51 to −51° with a step of 3° by SerialEM software.[51] The defocus was set as −5.0 μm when imaging. For each series, the total exposure dose was ∼100 $e/Å^2$, and the pixel size was 1.77 Å. The title series was imported into IMOD[52] for alignment and reconstruction. The final reconstruction was visualized and analyzed in UCSF Chimera.

Characterization of Graphene Membranes. The HAADF images of Janus bilayer graphene membranes were acquired by monochromatic Nion U-HERMES 200 electron microscope operated at 60 kV. The convergence semiangle ($\alpha/2$) was 35 mrad, and the collection semiangle ($\beta/2$) was 80−210 mrad. The raw images were further convoluted by a two-dimensional Gaussian function (Gaussian blur) to minimize the noise and improve the contrast. Raman spectrometer (532 nm, LabRAM HR-800, Horiba), SEM (acceleration voltage, 1−2 kV; Hitachi S-4800), cryo-SEM (Helios NanoLab G3 UC, ThermoFisher Scientific, equipped with a Quorum PP3010T refrigeration system), and water contact angle measurement (Dataphysics OCA 20) were used to investigate the structures and properties of graphene membranes.

AFM Nanoindentation. The mechanical properties of suspended graphene membranes were measured by nanoindentation experiments using Asylum Cypher ES atomic force microscopy. A single-crystal diamond probe with a tip radius of approximately 10 nm was used, and the cantilever stiffness was 30.85 N m^{-1} calibrated using the Sader method.[53] A constant deflection rate of 4 μm s^{-1} was used in all of the tests.

The prestress and elastic modulus were extracted from the indentation force *vs* depth data, using the previous model by Lee *et al.*:[54]

$$F = (\pi\sigma_0^{2D})\delta + \left(Et\frac{q^3}{r^2}\right)\delta^3$$

where F is the applied load; σ_0^{2D} is the two-dimensional prestress of nanosheets; δ is the indentation depth; r is the radius of microwells; and t is the nanosheet thickness. The dimensionless constant $q = 1/(1.05 - 0.15\upsilon_p - 0.16\upsilon_p^2)$, in which $\upsilon_p = 0.165$, is the Poisson ratio for graphene.[54]

Deposition of Lithium Dendrites onto the Janus Bilayer Graphene Membranes. Lithium dendrites are deposited on Janus bilayer graphene grids through an *in situ* electrochemical method. CR2016-type coin cells were assembled in a glovebox filled with argon. A bilayer Janus graphene grid was placed on a copper foil current collector as the working electrode paired with a piece of lithium metal as counter/reference electrode. 1.0 M $LiPF_6$ in ethylene carbonate, dimethyl carbonate, and diethyl carbonate (1:1:1 EC/DMC/DEC in volume, Guotaihuarong Co. Ltd.) was added as an electrolyte. The amount of electrolyte is controlled as 40 μL. Lithium deposition on the graphene grid was conducted in a LAND CT 2001A battery system at 0.25 mA cm^{-2} for 4 h to achieve an areal capacity of 1 mAh cm^{-2}.

Stability Test of Graphene Membranes. The graphene membrane was continuously radiated at the same position under the electron beam with a dose rate of ∼204.76 $(e/Å^2)/s$ in Tecnai F20 microscopy (200 kV), and we discretely collected its selected area electron diffraction patterns on a CCD camera (Gatan US4000) from 0 to 70 min. Afterward, we calculated the relative diffraction intensity defined by the ratio of the integrated intensity of the third-order diffraction spots over that of the first-order diffraction spots and plotted it *vs* electron dose to demonstrate the stability of the graphene grid under the electron beam.

ASSOCIATED CONTENT

Supporting Information

The Supporting Information is available free of charge at https://pubs.acs.org/doi/10.1021/acsnano.1c06233.

Figures showing additional atomic-resolution images of bilayer Janus graphene, water contact angle measurements, cryo-SEM characterizations, defect density measurements, AFM nanoindentation, coverage of bilayer Janus graphene, electron-beam resistance of bilayer Janus graphene, and cryo-EM images of proteins on bilayer Janus graphene (PDF)

https://doi.org/10.1021/acsnano.1c06233
ACS Nano 2021, 15, 16562−16571

AUTHOR INFORMATION

Corresponding Authors

Hailin Peng − *Center for Nanochemistry, Beijing Science and Engineering Center for Nanocarbons, Beijing National Laboratory for Molecular Sciences, College of Chemistry and Molecular Engineering and Academy for Advanced Interdisciplinary Studies, Peking University, Beijing 100871, China; Beijing Graphene Institute (BGI), Beijing 100095, China;* orcid.org/0000-0003-1569-0238; Email: hlpeng@pku.edu.cn

Hong-Wei Wang − *Ministry of Education Key Laboratory of Protein Sciences, Beijing Advanced Innovation Center for Structural Biology, School of Life Sciences, Tsinghua-Peking Joint Center for Life Sciences, and Beijing Frontier Research Center for Biological Structures, Tsinghua University, Beijing 100084, China;* orcid.org/0000-0001-9494-8780; Email: hongweiwang@tsinghua.edu.cn

Xiaoding Wei − *State Key Laboratory for Turbulence and Complex System, Department of Mechanics and Engineering Science, College of Engineering and Beijing Innovation Center for Engineering Science and Advanced Technology, Peking University, Beijing 100871, China;* orcid.org/0000-0002-5173-4923; Email: xdwei@pku.edu.cn

Authors

Liming Zheng − *Center for Nanochemistry, Beijing Science and Engineering Center for Nanocarbons, Beijing National Laboratory for Molecular Sciences, College of Chemistry and Molecular Engineering, Peking University, Beijing 100871, China*

Nan Liu − *Ministry of Education Key Laboratory of Protein Sciences, Beijing Advanced Innovation Center for Structural Biology, School of Life Sciences, Tsinghua University, Beijing 100084, China*

Ying Liu − *State Key Laboratory for Turbulence and Complex System, Department of Mechanics and Engineering Science, College of Engineering and Beijing Innovation Center for Engineering Science and Advanced Technology, Peking University, Beijing 100871, China*

Ning Li − *International Center for Quantum Materials and Electron Microscopy Laboratory, School of Physics and Academy for Advanced Interdisciplinary Studies, Peking University, Beijing 100871, China*

Jincan Zhang − *Center for Nanochemistry, Beijing Science and Engineering Center for Nanocarbons, Beijing National Laboratory for Molecular Sciences, College of Chemistry and Molecular Engineering and Academy for Advanced Interdisciplinary Studies, Peking University, Beijing 100871, China*

Chongzhen Wang − *Center for Nanochemistry, Beijing Science and Engineering Center for Nanocarbons, Beijing National Laboratory for Molecular Sciences, College of Chemistry and Molecular Engineering, Peking University, Beijing 100871, China; Department of Chemical and Biomolecular Engineering, University of California, Los Angeles, Los Angeles, California 90095, United States*

Wenqing Zhu − *State Key Laboratory for Turbulence and Complex System, Department of Mechanics and Engineering Science, College of Engineering and Beijing Innovation Center for Engineering Science and Advanced Technology, Peking University, Beijing 100871, China*

Yanan Chen − *Ministry of Education Key Laboratory of Protein Sciences, Beijing Advanced Innovation Center for Structural Biology, School of Life Sciences, Tsinghua University, Beijing 100084, China; School of Materials Science and Engineering, Tianjin University, Tianjin 300072, China;* orcid.org/0000-0002-6346-6372

Dongchen Ying − *Center for Nanochemistry, Beijing Science and Engineering Center for Nanocarbons, Beijing National Laboratory for Molecular Sciences, College of Chemistry and Molecular Engineering, Peking University, Beijing 100871, China*

Jie Xu − *Ministry of Education Key Laboratory of Protein Sciences, Beijing Advanced Innovation Center for Structural Biology, School of Life Sciences and Tsinghua-Peking Joint Center for Life Sciences, Tsinghua University, Beijing 100084, China*

Zi Yang − *Ministry of Education Key Laboratory of Protein Sciences, Beijing Advanced Innovation Center for Structural Biology, School of Life Sciences and Tsinghua-Peking Joint Center for Life Sciences, Tsinghua University, Beijing 100084, China*

Xiaoyin Gao − *Center for Nanochemistry, Beijing Science and Engineering Center for Nanocarbons, Beijing National Laboratory for Molecular Sciences, College of Chemistry and Molecular Engineering, Peking University, Beijing 100871, China*

Jilin Tang − *Center for Nanochemistry, Beijing Science and Engineering Center for Nanocarbons, Beijing National Laboratory for Molecular Sciences, College of Chemistry and Molecular Engineering and Academy for Advanced Interdisciplinary Studies, Peking University, Beijing 100871, China*

Xiaoge Wang − *Center for Nanochemistry, Beijing Science and Engineering Center for Nanocarbons, Beijing National Laboratory for Molecular Sciences, College of Chemistry and Molecular Engineering, Peking University, Beijing 100871, China*

Zibin Liang − *Beijing Key Laboratory for Theory and Technology of Advanced Battery Materials, School of Materials Science and Engineering, Peking University, Beijing 100871, China*

Ruqiang Zou − *Beijing Key Laboratory for Theory and Technology of Advanced Battery Materials, School of Materials Science and Engineering, Peking University, Beijing 100871, China;* orcid.org/0000-0003-0456-4615

Yuzhang Li − *Department of Chemical and Biomolecular Engineering, University of California, Los Angeles, Los Angeles, California 90095, United States;* orcid.org/0000-0002-1502-7869

Peng Gao − *International Center for Quantum Materials and Electron Microscopy Laboratory, School of Physics, Peking University, Beijing 100871, China; Collaborative Innovation Center of Quantum Matter, Beijing 100871, China;* orcid.org/0000-0003-0860-5525

Complete contact information is available at: https://pubs.acs.org/10.1021/acsnano.1c06233

Author Contributions

L.Z., N. Liu, and Y. Liu contributed equally to this work. H.P. and H.-W.W. conceived the project. L.Z. and N. Liu coordinated the experiments. Y. Liu. and X. Wei. performed the MD simulation. L.Z. prepared and characterized the bilayer Janus graphene membranes. N. Liu, L.Z., J.X., Z.Y., and Y.C. carried out the cryo-EM characterizations and analysis. N. Li

https://doi.org/10.1021/acsnano.1c06233
ACS Nano 2021, 15, 16562−16571

and P.G. carried out the atomic-resolution STEM images of graphene membranes. J.T. and X.G. synthesized the bilayer graphene films. W.Z., L.Z., and X. Wei carried out the AFM nanoindentation. D.Y. and L.Z. performed the Raman characterizations. J.Z., Z.L., and R.Z. measured the wettability. L.Z., C.W., X. Wang, and Y. Li. contributed to the cryo-TEM characterization of Li dentrite. H.P., L.Z., N. Liu. and H.-W.W. wrote the manuscript. All authors discussed the results and commented on the manuscript. All authors have given approval to the final version of the manuscript.

Notes

The authors declare no competing financial interest.

ACKNOWLEDGMENTS

We thank X. M. Li, J. L. Lei, and F. Yang at Tsinghua University Cryo-EM Facility of China National Center for Protein Sciences (Beijing) for their assistance in cryo-SEM characterization and Y. Zhao and Y. Hou for fruitful discussions and assistance in experiments. We are grateful to the Electron Microscopy Laboratory at Peking University for the use of electron microscopes. We thank Shuimu BioSciences Co. for the support of cryo-EM data collaction. This work was accomplished using the service provided by the Peking University Analytical Instrumentation Center. N. Liu. thanks the Shuimu Tsinghua Scholar Program for support. We acknowledge financial support from the National Basic Research Program of China (Grant No. 2016YFA0200101 to H.P. and Grant No. 2016YFA0501100 to H.-W.W.), the National Natural Science Foundation of China (Grant Nos. 52021006 and 21525310 to H.P., Grant No. 31825009 to H.-W.W., Grant No. 11974023 to P.G., and Grant Nos. 11772003, 11890681, and 11988102 to X. Wei).

REFERENCES

(1) Cheng, Y. F. Single-Particle Cryo-EM at Crystallographic Resolution. *Cell* **2015**, *161*, 450−457.

(2) Yip, K. M.; Fischer, N.; Paknia, E.; Chari, A.; Stark, H. Atomic-Resolution Protein Structure Determination by Cryo-EM. *Nature* **2020**, *587*, 157.

(3) Nakane, T.; Kotecha, A.; Sente, A.; McMullan, G.; Masiulis, S.; Brown, P. M. G. E.; Grigoras, I. T.; Malinauskaite, L.; Malinauskas, T.; Miehling, J.; Uchanski, T.; Yu, L. B.; Karia, D.; Pechnikova, E. V.; de Jong, E.; Keizer, J.; Bischoff, M.; McCormack, J.; Tiemeijer, P.; Hardwick, S. W.; et al. Single-Particle Cryo-EM at Atomic Resolution. *Nature* **2020**, *587*, 152.

(4) Bai, R.; Wan, R. X.; Yan, C. Y.; Jia, Q.; Lei, J. L.; Shi, Y. G. Mechanism of Spliceosome Remodeling by the ATPase/Helicase Prp2 and Its Coactivator Spp2. *Science* **2021**, *371*, eabe8863.

(5) Li, Y. Z.; Li, Y. B.; Pei, A. L.; Yan, K.; Sun, Y. M.; Wu, C. L.; Joubert, L. M.; Chin, R.; Koh, A. L.; Yu, Y.; Perrino, J.; Butz, B.; Chu, S.; Cui, Y. Atomic Structure of Sensitive Battery Materials and Interfaces Revealed by Cryo-Electron Microscopy. *Science* **2017**, *358*, 506−510.

(6) Yu, Z.; Wang, H. S.; Kong, X.; Huang, W.; Tsao, Y. C.; Mackanic, D. G.; Wang, K. C.; Wang, X. C.; Huang, W. X.; Choudhury, S.; Zheng, Y.; Amanchukwu, C. V.; Hung, S. T.; Ma, Y. T.; Lomeli, E. G.; Qin, J.; Cui, Y.; Bao, Z. N. Molecular Design for Electrolyte Solvents Enabling Energy-Dense and Long-Cycling Lithium Metal Batteries. *Nat. Energy* **2020**, *5*, 526−533.

(7) Boyle, D. T.; Huang, W.; Wang, H. S.; Li, Y. Z.; Chen, H.; Yu, Z.; Zhang, W. B.; Bao, Z. N.; Cui, Y. Corrosion of Lithium Metal Anodes during Calendar Ageing and Its Microscopic Origins. *Nat. Energy* **2021**, *6*, 487−494.

(8) Li, Y. B.; Zhou, W. J.; Li, Y. Z.; Huang, W. X.; Zhang, Z. W.; Chen, G. X.; Wang, H. S.; Wu, G. H.; Rolston, N.; Vila, R.; Chiu, W.; Cui, Y. Unravelling Degradation Mechanisms and Atomic Structure of Organic-Inorganic Halide Perovskites by Cryo-EM. *Joule* **2019**, *3*, 2854−2866.

(9) Li, Y. Z.; Wang, K. C.; Zhou, W. J.; Li, Y. B.; Vila, R.; Huang, W.; Wang, H. X.; Chen, G. X.; Wu, G. H.; Tsao, Y. C.; Wang, H. S.; Sinclair, R.; Chiu, W.; Cui, Y. Cryo-EM Structures of Atomic Surfaces and Host-Guest Chemistry in Metal-Organic Frameworks. *Matter* **2019**, *1*, 428−438.

(10) Glaeser, R. M. Preparing Better Samples for Cryo-Electron Microscopy: Biochemical Challenges Do Not End with Isolation and Purification. *Annu. Rev. Biochem.* **2021**, *90*, 451−474.

(11) Naydenova, K.; Peet, M. J.; Russo, C. J. Multifunctional Graphene Supports for Electron Cryomicroscopy. *Proc. Natl. Acad. Sci. U. S. A.* **2019**, *116*, 11718−11724.

(12) Fan, X.; Wang, J.; Zhang, X.; Yang, Z.; Zhang, J. C.; Zhao, L. Y.; Peng, H. L.; Lei, J. L.; Wang, H. W. Single Particle Cryo-EM Reconstruction of 52 kDa Streptavidin at 3.2 Angstrom Resolution. *Nat. Commun.* **2019**, *10*, 2386.

(13) Han, Y. M.; Fan, X.; Wang, H. Z.; Zhao, F.; Tully, C. G.; Kong, J.; Yao, N.; Yan, N. High-Yield Monolayer Graphene Grids for Near-Atomic Resolution Cryoelectron Microscopy. *Proc. Natl. Acad. Sci. U. S. A.* **2020**, *117*, 1009−1014.

(14) Zheng, L.; Chen, Y.; Li, N.; Zhang, J.; Liu, N.; Liu, J.; Dang, W.; Deng, B.; Li, Y.; Gao, X.; et al. Robust Ultraclean Atomically Thin Membranes for Atomic-Resolution Electron Microscopy. *Nat. Commun.* **2020**, *11*, 541.

(15) Liu, N.; Zhang, J. C.; Chen, Y. A.; Liu, C.; Zhang, X.; Xu, K.; Wen, J.; Luo, Z. P.; Chen, S. L.; Gao, P.; Jia, K. C.; Liu, Z. F.; Peng, H. L.; Wang, H. W. Bioactive Functionalized Monolayer Graphene for High-Resolution Cryo-Electron Microscopy. *J. Am. Chem. Soc.* **2019**, *141*, 4016−4025.

(16) D'Imprima, E.; Floris, D.; Joppe, M.; Sanchez, R.; Grininger, M.; Kuhlbrandt, W. Protein Denaturation at the Air-Water Interface and How to Prevent It. *eLife* **2019**, *8*, No. e42747.

(17) Russo, C. J.; Passmore, L. A. Controlling Protein Adsorption on Graphene for Cryo-EM Using Low-Energy Hydrogen Plasmas. *Nat. Methods* **2014**, *11*, 773−773.

(18) Liu, N.; Zheng, L.; Xu, J.; Wang, J.; Hu, C.; Lan, J.; Zhang, X.; Zhang, J.; Xu, K.; Cheng, H.; et al. Reduced Graphene Oxide Membrane as Supporting Film for High-Resolution Cryo-EM. *Biophys. Rep.* **2021**, *7*, 227−238.

(19) Palovcak, E.; Wang, F.; Zheng, S. Q.; Yu, Z. L.; Li, S.; Betegon, M.; Bulkley, D.; Agard, D. A.; Cheng, Y. F. A Simple and Robust Procedure for Preparing Graphene-Oxide Cryo-EM Grids. *J. Struct. Biol.* **2018**, *204*, 80−84.

(20) Wang, F.; Liu, Y. X.; Yu, Z. L.; Li, S.; Feng, S. J.; Cheng, Y. F.; Agard, D. A. General and Robust Covalently Linked Graphene Oxide Affinity Grids for High-Resolution Cryo-EM. *Proc. Natl. Acad. Sci. U. S. A.* **2020**, *117*, 24269−24273.

(21) Pantelic, R. S.; Suk, J. W.; Magnuson, C. W.; Meyer, J. C.; Wachsmuth, P.; Kaiser, U.; Ruoff, R. S.; Stahlberg, H. Graphene: Substrate Preparation and Introduction. *J. Struct. Biol.* **2011**, *174*, 234−238.

(22) Rhinow, D.; Weber, N. E.; Turchanin, A.; Golzhauser, A.; Kuhlbrandt, W. Single-Walled Carbon Nanotubes and Nanocrystalline Graphene Reduce Beam-Induced Movements in High-Resolution Electron Cryo-Microscopy of Ice-Embedded Biological Samples. *Appl. Phys. Lett.* **2011**, *99*, 133701.

(23) Scherr, J.; Tang, Z.; Kullmer, M.; Balser, S.; Scholz, A. S.; Winter, A.; Parey, K.; Rittner, A.; Grininger, M.; Zickermann, V.; Rhinow, D.; Terfort, A.; Turchanin, A. Smart Molecular Nanosheets for Advanced Preparation of Biological Samples in Electron Cryo-Microscopy. *ACS Nano* **2020**, *14* (8), 9972−9978.

(24) Zandiatashbar, A.; Lee, G. H.; An, S. J.; Lee, S.; Mathew, N.; Terrones, M.; Hayashi, T.; Picu, C. R.; Hone, J.; Koratkar, N. Effect of Defects on the Intrinsic Strength and Stiffness of Graphene. *Nat. Commun.* **2014**, *5*, 3186.

https://doi.org/10.1021/acsnano.1c06233
ACS Nano 2021, 15, 16562−16571

(25) Kim, K.; Park, H. J.; Woo, B. C.; Kim, K. J.; Kim, G. T.; Yun, W. S. Electric Property Evolution of Structurally Defected Multilayer Graphene. *Nano Lett.* **2008**, *8*, 3092−3096.
(26) Lin, L.; Deng, B.; Sun, J. Y.; Peng, H. L.; Liu, Z. F. Bridging the Gap between Reality and Ideal in Chemical Vapor Deposition Growth of Graphene. *Chem. Rev.* **2018**, *118* (18), 9281−9343.
(27) Zhang, J.; Jia, K.; Lin, L.; Zhao, W.; Quang, H. T.; Sun, L. Z.; Li, T. R.; Li, Z. Z.; Liu, X. T.; Zheng, L. M.; et al. Large-Area Synthesis of Superclean Graphene *via* Selective Etching of Amorphous Carbon with Carbon Dioxide. *Angew. Chem., Int. Ed.* **2019**, *58*, 14446−14451.
(28) Glaeser, R. M. Proteins, Interfaces, and Cryo-EM Grids. *Curr. Opin. Colloid Interface Sci.* **2018**, *34*, 1−8.
(29) Zhou, H. L.; Yu, W. J.; Liu, L. X.; Cheng, R.; Chen, Y.; Huang, X. Q.; Liu, Y.; Wang, Y.; Huang, Y.; Duan, X. F. Chemical Vapour Deposition Growth of Large Single Crystals of Monolayer and Bilayer Graphene. *Nat. Commun.* **2013**, *4*, 2096.
(30) Zhang, J. C.; Lin, L.; Sun, L. Z.; Huang, Y. C.; Koh, A. L.; Dang, W. H.; Yin, J. B.; Wang, M. Z.; Tan, C. W.; Li, T. R.; Tan, Z. J.; Liu, Z. F.; Peng, H. L. Clean Transfer of Large Graphene Single Crystals for High-Intactness Suspended Membranes and Liquid Cells. *Adv. Mater.* **2017**, *29*, 1700639.
(31) Shih, C. J.; Wang, Q. H.; Lin, S. C.; Park, K. C.; Jin, Z.; Strano, M. S.; Blankschtein, D. Breakdown in the Wetting Transparency of Graphene. *Phys. Rev. Lett.* **2012**, *109*, 176101.
(32) Rafiee, J.; Mi, X.; Gullapalli, H.; Thomas, A. V.; Yavari, F.; Shi, Y. F.; Ajayan, P. M.; Koratkar, N. A. Wetting Transparency of Graphene. *Nat. Mater.* **2012**, *11*, 217−222.
(33) Driskill, J.; Vanzo, D.; Bratko, D.; Luzar, A. Wetting Transparency of Graphene in Water. *J. Chem. Phys.* **2014**, *141*, 18C517.
(34) Cancado, L. G.; Jorio, A.; Ferreira, E. H. M.; Stavale, F.; Achete, C. A.; Capaz, R. B.; Moutinho, M. V. O.; Lombardo, A.; Kulmala, T. S.; Ferrari, A. C. Quantifying Defects in Graphene *via* Raman Spectroscopy at Different Excitation Energies. *Nano Lett.* **2011**, *11*, 3190−3196.
(35) Hofer, C.; Skakalova, V.; Gorlich, T.; Tripathi, M.; Mittelberger, A.; Mangler, C.; Monazam, M. R. A.; Susi, T.; Kotakoski, J.; Meyer, J. C. Direct Imaging of Light-Element Impurities in Graphene Reveals Triple-Coordinated Oxygen. *Nat. Commun.* **2019**, *10*, 4570.
(36) Markowitz, M. M.; Boryta, D. A. Lithium Metal-Gas Reactions. *J. Chem. Eng. Data* **1962**, *7*, 586−591.
(37) Noble, A. J.; Wei, H.; Dandey, V. P.; Zhang, Z. N.; Tan, Y. Z.; Potter, C. S.; Carragher, B. Reducing Effects of Particle Adsorption to the Air-Water Interface in Cryo-EM. *Nat. Methods* **2018**, *15*, 793.
(38) Noble, A. J.; Dandey, V. P.; Wei, H.; Brasch, J.; Chase, J.; Acharya, P.; Tan, Y. Z.; Zhang, Z. N.; Kim, L. Y.; Scapin, G.; et al. Routine Single Particle CryoEM Sample and Grid Characterization by Tomography. *eLife* **2018**, *7*, No. e34257.
(39) Naydenova, K.; Jia, P. P.; Russo, C. J. Cryo-EM with Sub-1 Angstrom Specimen Movement. *Science* **2020**, *370*, 223.
(40) Wang, B.; Luo, D.; Li, Z. C.; Kwon, Y.; Wang, M. H.; Goo, M.; Jin, S. W.; Huang, M.; Shen, Y. T.; Shi, H. F.; Ding, F.; Ruoff, R. S. Camphor-Enabled Transfer and Mechanical Testing of Centimeter-Scale Ultrathin Films. *Adv. Mater.* **2018**, *30*, 1800888.
(41) Glaeser, R. M.; McMullan, G.; Faruqi, A. R.; Henderson, R. Images of Paraffin Monolayer Crystals with Perfect Contrast: Minimization of Beam-Induced Specimen Motion. *Ultramicroscopy* **2011**, *111*, 90−100.
(42) Russo, C. J.; Passmore, L. A. Ultrastable Gold Substrates: Properties of a Support for High-Resolution Electron Cryomicroscopy of Biological Specimens. *J. Struct. Biol.* **2016**, *193*, 33−44.
(43) Li, Q.; Pellegrino, J.; Lee, D. J.; Tran, A. A.; Chaires, H. A.; Wang, R. X.; Park, J. E.; Ji, K. J.; Chow, D.; Zhang, N.; Brilot, A. F.; Biel, J. T.; van Zundert, G.; Borrelli, K.; Shinabarger, D.; Wolfe, C.; Murray, B.; Jacobson, M. P.; Muhle, E.; Chesneau, O.; et al. Synthetic Group A Streptogramin Antibiotics That Overcome Vat Resistance. *Nature* **2020**, *586*, 145.
(44) Plimpton, S. Fast Parallel Algorithms for Short-Range Molecular-Dynamics. *J. Comput. Phys.* **1995**, *117*, 1−19.
(45) Baskes, M. I. The Status Role of Modeling and Simulation in Materials Science and Engineering. *Curr. Opin. Solid State Mater. Sci.* **1999**, *4*, 273−277.
(46) Chenoweth, K.; van Duin, A. C. T.; Goddard, W. A. ReaxFF Reactive Force Field for Molecular Dynamics Simulations of Hydrocarbon Oxidation. *J. Phys. Chem. A* **2008**, *112*, 1040−1053.
(47) Lei, J. L.; Frank, J. Automated Acquisition of Cryo-Electron Micrographs for Single Particle Reconstruction on an FEI Tecnai Electron Microscope. *J. Struct. Biol.* **2005**, *150*, 69−80.
(48) Zheng, S. Q.; Palovcak, E.; Armache, J. P.; Verba, K. A.; Cheng, Y. F.; Agard, D. A. MotionCor2: Anisotropic Correction of Beam-Induced Motion for Improved Cryo-Electron Microscopy. *Nat. Methods* **2017**, *14*, 331−332.
(49) Rohou, A.; Grigorieff, N. CTFFIND4: Fast and Accurate Defocus Estimation from Electron Micrographs. *J. Struct. Biol.* **2015**, *192*, 216−221.
(50) Scheres, S. H. W. RELION: Implementation of a Bayesian Approach to Cryo-EM Structure Determination. *J. Struct. Biol.* **2012**, *180*, 519−530.
(51) Mastronarde, D. N. Automated Electron Microscope Tomography Using Robust Prediction of Specimen Movements. *J. Struct. Biol.* **2005**, *152*, 36−51.
(52) Kremer, J. R.; Mastronarde, D. N.; McIntosh, J. R. Computer Visualization of Three-Dimensional Image Data Using IMOD. *J. Struct. Biol.* **1996**, *116*, 71−76.
(53) Higgins, M. J.; Proksch, R.; Sader, J. E.; Polcik, M.; Mc Endoo, S.; Cleveland, J. P.; Jarvis, S. P. Noninvasive Determination of Optical Lever Sensitivity in Atomic Force Microscopy. *Rev. Sci. Instrum.* **2006**, *77*, No. 013701.
(54) Lee, C.; Wei, X.; Kysar, J. W.; Hone, J. Measurement of the Elastic Properties and Intrinsic Strength of Monolayer Graphene. *Science* **2008**, *321*, 385−388.

https://doi.org/10.1021/acsnano.1c06233
ACS Nano 2021, 15, 16562−16571